Pore-scale modeling of multiphase reactive transport with phase transitions and dissolution-precipitation processes in closed systems

Li Chen,[1,2] Qinjun Kang,[2,*] Bruce A. Robinson,[3] Ya-Ling He,[1] and Wen-Quan Tao[1]

[1]*Key Laboratory of Thermo-Fluid Science and Engineering of MOE, School of Energy and Power Engineering, Xi'an Jiaotong University, Xi'an, Shaanxi 710049, China*
[2]*Computational Earth Science Group (EES-16), Los Alamos National Laboratory, Los Alamos, New Mexico 87545, USA*
[3]*Civilian Nuclear Programs, Los Alamos National Laboratory, Los Alamos, New Mexico 87545, USA*

A pore-scale model based on the lattice Boltzmann (LB) method is developed for multiphase reactive transport with phase transitions and dissolution-precipitation processes. The model combines the single-component multiphase Shan-Chen LB model [X. Shan and H. Chen, Phys. Rev. E **47**, 1815 (1993)], the mass transport LB model [S. P. Sullivan *et al.*, Chem. Eng. Sci. **60**, 3405 (2005)], and the dissolution-precipitation model [Q. Kang *et al.*, J. Geophys. Res. **111**, B05203 (2006)]. Care is taken to handle information on computational nodes undergoing solid-liquid or liquid-vapor phase changes to guarantee mass and momentum conservation. A general LB concentration boundary condition is proposed that can handle various concentration boundaries including reactive and moving boundaries with complex geometries. The pore-scale model can capture coupled nonlinear multiple physicochemical processes including multiphase flow with phase separations, mass transport, chemical reactions, dissolution-precipitation processes, and dynamic evolution of the pore geometries. The model is validated using several multiphase flow and reactive transport problems and then used to study the thermal migration of a brine inclusion in a salt crystal. Multiphase reactive transport phenomena with phase transitions between liquid-vapor phases and dissolution-precipitation processes of the salt in the closed inclusion are simulated and the effects of the initial inclusion size and temperature gradient on the thermal migration are investigated.

PACS number(s): 47.11.Qr

I. INTRODUCTION

Reactive transport processes in porous media are pervasive in industrial and natural systems. These include the recovery of oil, the storage of carbon dioxide (CO_2) in the subsurface [1], precipitation patterns in Liesegang phenomena [2], and the water flooding issue in proton exchange membrane fuel cells (PEMFCs) [3,4]. These reactive transport processes are often associated with multiphase flow, which can be single-component multiphase (such as water vapor and liquid water) [5] or multicomponent multiphase flow (such as air-liquid water) [6] and may contain phase transitions [7]. Such reactive transport processes can also lead to the dynamic evolution of pore geometries due to dissolution or precipitation, leading to different dissolution [8] or precipitation patterns [2]. The changes of the pore geometries may in turn significantly and continuously modify the transport properties of the porous media, such as the permeability [9–11]. Such reactive transport processes can also alter the physical properties of the related immiscible or miscible fluids and thus can modify the flow patterns or trigger new flow patterns [12]. Most of these reactive transport processes originate from the pore scale, but often present multiscale characteristics in which the length or time scale involved covers a wide range and the dominant factors of the processes change over time, making the situation more complex [13,14]. Therefore, to accurately model these processes at the scales of interest, it is important to greatly enhance our understanding and capability to simulate these processes at the pore scale as a precursor to incorporating those pore-scale processes into continuum-scale descriptions.

Different numerical methods have been used to investigate pore-scale multiphase reactive transport processes, including the direct numerical simulation method [15], pore-network model [16,17], lattice Boltzmann method (LBM) [1,3,8,9,18], and smoothed particle hydrodynamics [19,20]. Each of these methods has its own advantages and disadvantages. We base our model on the LBM, which is well suited for solving fluid flow in complex geometries and has been successfully used in the study of flow in porous media [21]. Furthermore, the kinetic nature of the LBM enables it to conveniently represent microscopic interactions between different fluids, thereby facilitating the automatic tracking of the fluid interfaces in a multiphase system [22,23]. In contrast, other multiphase modeling methods such as the level set method and the volume of fluid method rely on additional auxiliary algorithms to track the fluid interfaces. The fluid-solid interactions can also be implemented conveniently in the LBM without including additional complex kernels [21,24].

To account for the dynamic evolution of the solid-fluid interface, several models have been developed to track the moving solid-fluid interface, some of which are directly related to models of tracking fluid interfaces. These models can be classified in two groups: the diffusion interface model and the sharp interface model. In the diffusion interface model, a scalar field is used as a phase indicator. The characteristic feature of the diffusion interface model is that the scalar varies continuously and smoothly across the fluid-solid interface [25]. Similarly, a scalar field is also solved as the phase indicator in the front-capturing method embodied in the sharp interface model. Typical examples are the level set method [11] and the volume of fluid method [26]. However, unlike the smooth transition of the scalar field across the phase

*qkang@lanl.gov

interface in the diffusion interface model, in the sharp interface model the scalar field generally alters sharply across the phase interfaces and usually additional auxiliary algorithms are required to reconstruct the interfaces near the phase interface [11,26]. Another category of the sharp interface model is the front-tracking method. In this method, the evolving solid-fluid interfaces in dissolution (or melting) and precipitation (or solidification) problems are represented by connected Lagrangian marker points that are updated at each computational time step [27,28]. Since in most cases there is no fluid flow and mass transport in the solid phase, and flow at the solid-fluid interfaces is subject to a no-slip condition, the front-tracking method is especially suitable for tracking the solid-fluid interfaces. Kang *et al*. [28] developed a volume of pixel (VOP) method, which is a type of front-tracking method, to track the solid-fluid interface. In the VOP method, the entire domain is divided into pixels (or computational nodes). Each pixel is assigned a value representing the volume of the solid phase. At each time step, the volume of solid pixels at the solid-fluid interfaces is updated based on the local dissolution or precipitation rate. If the volume of a solid pixel decreases to zero due to dissolution (or melting), this solid pixel is removed and changed into a fluid pixel. In contrast, if the volume of a solid pixel increases to a threshold value due to precipitation (or solidification), one of its neighboring fluid pixels is changed into a solid pixel. Note that only the solid pixels at the solid-fluid interfaces require treatment since the reactions only take place at the solid-fluid interface. In the simplest version of the VOP method, the solid-fluid interface is stepwise [28]. However, one can also use some additional geometrical algorithms around the interfaces to obtain curved interfaces [27]. The VOP method has many advantages such as a clear physical concept, simple and stable arithmetic, easy implementation of various kinds of surface reactions, and flexible coupling with different nucleation and crystal growth mechanisms. For this reason, the method has been used successfully to predict many moving solid-fluid interface phenomena such as crystal growth [18], rock dissolution due to acid injection [9], Liesegang bands or rings [2], and dissolution and precipitation in CO_2 sequestration [1,29].

There have been a few numerical studies to investigate reactive flow with an evolving solid-fluid interface at the pore scale. Single-phase fluid flow and reactive transport with dissolution and precipitation was studied by Kang *et al*. [8,9] in which LBM was used to simulate flow, transport, and reaction and the VOP method was adopted to track the moving solid-fluid interfaces due to dissolution and precipitation. They predicted the relationship between permeability and porosity under different Péclet number (Pe) (representing the relative strength of convection to diffusion) and Damköhler number (Da) (representing the relative strength of reaction to diffusion). Li *et al*. [11] studied a similar problem using a projection method to solve the fluid flow and the level set method to track the solid-fluid interfaces. In addition, Luo *et al*. [25] implemented a model using a diffuse interface method to track the solid-fluid interface, in which they also considered the natural convection caused by concentration gradients. Later, Kang *et al*. extended their model to multicomponent systems [28] and used the model to study reactive transport processes associated with geological CO_2 sequestration [1].

The numerical studies of multiphase fluid flow and reactive transport with moving solid-fluid interfaces are sparse in the literature [30]. Recently, Parmigiani *et al*. [30] used the LBM to study the process of injection of a nonwetting fluid into a wetting fluid coupled with dynamic evolution of the solid geometries. While they suggested that their model can be used for reactive transport with dissolution or precipitation, the study demonstrated only melting of the solid phase. From this review, it can be seen that further studies are warranted to understand multiphase reactive transport processes with moving solid-fluid interfaces.

The present study is primarily motivated by thermal-gradient migration of brine inclusions in a single crystal of salt [31]. Salt deposits have been considered as an attractive disposal medium for heat-generating wastes such as used nuclear fuel. However, because thermally driven migration of brine could have deleterious effects on the performance of waste canisters or impact the mechanical behavior of the salt medium [32], models of the brine migration process are needed to ensure the safe disposal of heat-generating nuclear waste in salt. During the migration, several coupled physicochemical processes take place including multiphase fluid flow with phase transition, heat transfer, mass transport, heterogeneous reactions, dissolution and precipitation, and dynamic evolution of the pore geometry. The challenges of numerical simulation of such a problem at the pore scale are to accurately model the coexistence of three phases (gas, liquid, and solid phases), predict dynamic evolution of phase interfaces (liquid-gas interfaces due to fluid flow and liquid-solid interfaces due to dissolution and precipitation), and consider the complex interplay between the multiple processes. In addition, brine inclusion inside the salt crystal is a closed system, which requires careful treatment to ensure strict mass and momentum conservation.

The goal of the present study is to establish a pore-scale model that helps gain a fundamental understanding of coupled nonlinear, nonequilibrium multiphase reactive transport including liquid-vapor phase transitions and dissolution-precipitation processes. We develop a pore-scale model that combines the single-component multiphase Shan-Chen model [22,23], a lattice Boltzmann (LB) mass transport model [3,33], and a dissolution and precipitation model [9,18]. To guarantee mass and momentum conservation in a closed system, we develop schemes for handling flow and transport information associated with computational nodes undergoing liquid-vapor or liquid-solid phase changes. We also propose a general LB concentration boundary condition that can handle various concentration boundaries including complex moving and reactive boundaries. The pore-scale model established from these basic building blocks can be used to comprehensively simulate multiphase reactive transport problems including multiphase flow with phase transitions, solute transport, heat transfer, chemical reactions, dissolution and precipitation, and dynamic evolution of pore structures. The pore-scale model developed can also be used to simulate multiphase reactive transport during geological storage of CO_2 and to simulate two-phase reactive flows in PEMFCs. Currently, our model is restricted to two-dimensional applications, but it should be relatively straightforward to extend this model to three dimensions.

In the remainder of the paper we describe the physico-chemical model (Sec. II) established and briefly introduce the multiphase reactive transport processes involved. In Sec. III we present the single-component multiphase Shan-Chen model, the mass transport LB model, and the dissolution-precipitation model adopted in the present study. We validate our models in Sec. IV. In Sec. V we present simulation results on thermal migration of a brine inclusion in a salt crystal. We then conclude with a summary and suggested avenues for future work in Sec. VI.

II. GENERAL PHYSICOCHEMICAL PROCESSES

If heat-generating nuclear waste is disposed in salt, the salt in the vicinity of the waste will heat up and a temperature gradient will be established between the waste and the salt distant from the waste. Our study is motivated by the thermal gradient migration of a brine inclusion in a single crystal of salt under these circumstances. The physicochemical problem is schematically shown in Fig. 1 and can be generally described as follows. A solid matrix (the single crystal of salt) contains an intragranular inclusion of brine in chemical equilibrium with the solid salt. Then the solid matrix is subjected to a temperature gradient. The solubility of the salt increases as the temperature increases. Thus the salt dissolves on the hot side of the inclusion, then the dissolved salt transports through the fluid to the cold side, and finally the salt precipitates on the cold side. The net effect is the microscopic dynamic evolution of the geometries of the inclusion and the macroscopic migration of the inclusion toward the regions with higher temperature. During the migration process, the total volume of the inclusion may change due to unequal amounts of dissolution and precipitation. In a closed system, if the volume of the inclusion increases due to dissolution outpacing precipitation, at a certain critical condition the brine in the closed inclusion will separate into a vapor phase and a liquid phase, leading to two-phase flow in the inclusion. Based on the above description, the corresponding governing equations for the fluid flow, mass transport, and heat transfer are as follows:

$$\frac{\partial \rho}{\partial t} + (\mathbf{u} \cdot \nabla)\rho = 0, \tag{1a}$$
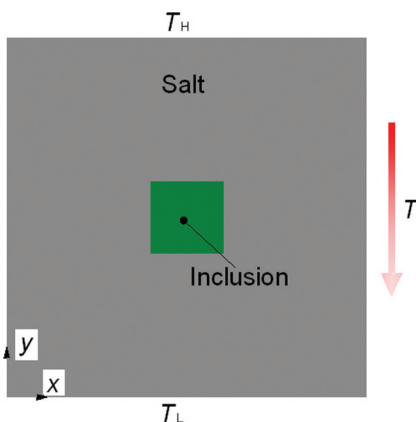
FIG. 1. (Color online) Schematic of the thermal migration of a brine inclusion in a salt crystal.

$$\frac{\partial \rho \mathbf{u}}{\partial t} + \rho \nabla \cdot (\mathbf{uu}) = -\nabla p + \nabla \cdot (\nabla \mu \mathbf{u}), \tag{1b}$$

$$\frac{\partial C_{aq}}{\partial t} + (\mathbf{u} \cdot \nabla)C_{aq} = D \Delta C_{aq}, \tag{1c}$$

$$\frac{\partial T}{\partial t} + (\mathbf{u} \cdot \nabla)T = \alpha \Delta T. \tag{1d}$$

In the above equations, t is time, ρ is the total density of the fluid mixture, $\mathbf{u}$ is the velocity, p is the pressure, μ is the dynamic viscosity, C_{aq} is the concentration of the dissolved salt in the solution, D is the diffusivity, T is the temperature, and α is the thermal diffusivity.

Clearly, the physicochemical problem under consideration is significantly complex, involving several coupled processes including multiphase flow with phase separation, heat transfer, mass transport, heterogeneous surface reactions, dissolution and precipitation, and dynamic evolution of the geometry of the inclusion. Such multiple coupled nonlinear physicochemical processes pose great challenges to numerical simulations. In the present study, two assumptions are adopted to make the numerical studies feasible: (i) when present, the phase transition during the thermal gradient migration of brine inclusion is approximated by a single-component multiphase system consisting of the liquid water phase in equilibrium with the vapor phase, neglecting the effect of the dissolved salt on the thermodynamics of the liquid-water–vapor system, and (ii) due to the small size of the inclusion compared to the solid matrix, the latent heat during the phase transition is neglected, as well as the effect of the inclusion on temperature distribution. As a result, the temperature field can be described by the heat conduction in the solid matrix.

The complex interactions of the multiple processes and the dynamic evolution of the complex interfaces between liquid-vapor-solid phases in the physicochemical problems mentioned above are described by a large set of nonlinear partial differential equations. Solving this set of equations with the common finite-element and finite-volume techniques is extremely challenging due to the complicated nonlinear characteristics as well as the complex structures. Alternatively, the LBM is more promising for solving such coupled nonlinear physicochemical problems at the pore scale because of its ability to account for complex structures and all relevant physicochemical processes. In the present study, the single-component multiphase Shan-Chen LB model, the mass transport LB model, and the VOP method are combined to study the multiphase reactive transport process with phase transitions and dissolution-precipitation processes.

III. NUMERICAL MODEL

A. Shan-Chen LB model for single-component multiphase flow

In the LB method, the motion of fluid is described by a set of particle distribution functions. Based on the simple and popular Bhatnagar-Gross-Krook collision operator [34], the evolution of the density distribution function is written as

$$f_i(\mathbf{x} + c\mathbf{e}_i \Delta t, t + \Delta t) - f_i(\mathbf{x},t) = -\frac{1}{\tau_\upsilon}\left[f_i(\mathbf{x},t) - f_i^{eq}(\mathbf{x},t)\right], \tag{2}$$

where $f_i(x,t)$ is the density distribution function at the lattice site **x** and time t, f^{eq} is the equilibrium distribution function, $c = \Delta x / \Delta t$ is the lattice speed with Δx and Δt the lattice spacing and time step, respectively, and τ_v is the dimensionless relaxation time. The discrete velocities $\mathbf{e}_i$ depend on the particular velocity model. For the D2Q9 model with nine velocity directions at a given point in two-dimensional space [35], $\mathbf{c}_i$ are given by

$$\mathbf{e}_i = \begin{cases} 0, & i = 0 \\ \left(\cos \left[\frac{(i-1)\pi}{2} \right], \sin \left[\frac{(i-1)\pi}{2} \right] \right), & i = 1,2,3,4 \\ \sqrt{2} \left(\cos \left[\frac{(i-5)\pi}{2} + \frac{\pi}{4} \right], \left[\frac{(i-5)\pi}{2} + \frac{\pi}{4} \right] \right), & i = 5,6,7,8. \end{cases}$$
$$(3)$$

The equilibrium distribution functions f^{eq} for the D2Q9 lattice are of the form

$$f_i^{eq} = \omega_i \rho \left[1 + \frac{3}{c^2} (\mathbf{e}_i \cdot \mathbf{u}) + \frac{9}{2c^4} (\mathbf{e}_i \cdot \mathbf{u})^2 - \frac{3}{2c^2} \mathbf{u}^2 \right],$$
$$(4)$$

where the weight factors ω_i are given by $\omega_0 = 4/9$, $\omega_{1-4} = 1/9$, and $\omega_{5-8} = 1/36$. The fluid density ρ and fluid velocity **u** can be obtained from the first and second moments of the particle distribution functions

$$\rho = \sum_i f_i, \tag{5a}$$

$$\rho \mathbf{u} = \sum_i f_i e_i. \tag{5b}$$

The viscosity in the lattice unit is related to the collision time by

$$\upsilon = c_s^2 (\tau_\upsilon - 0.5) \Delta t, \tag{6}$$

where c_s is the lattice sound speed.

Microscopically, the segregation of a fluid system into different phases results from the forces between molecules. In Shan and Chen's pseudopotential model, an interaction force (cohesive force) calculated from an effective mass ψ is introduced to model the molecule forces

$$\mathbf{F}_c = -G \psi(\mathbf{x}) \sum_{\alpha=1}^{N} w(|\mathbf{e}_\alpha|^2) \psi(\mathbf{x} + \mathbf{e}_\alpha) \mathbf{e}_\alpha, \tag{7}$$

where G reflects the interaction strength and $w(|\mathbf{e}^\alpha|^2)$ are the weights. If only the interactions of four nearest neighbors with $|\mathbf{e}^\alpha|^2 = 1$ and the four next-nearest neighbors $|\mathbf{e}^\alpha|^2 = 2$ are considered, $w(1) = 1/3$ and $w(2) = 1/12$.

Besides fluid-fluid interactions, there are also forces between the fluid and solid. The adhesion force between the fluid and the solid wall can be calculated by

$$\mathbf{F}_w = -w \psi(\mathbf{x}) \sum_{\alpha=1}^{N} w(|\mathbf{e}_\alpha|^2) s(\mathbf{x} + \mathbf{e}_\alpha) \mathbf{e}_\alpha, \tag{8}$$

where w determines the strength of the interaction between the fluid and the solid wall and s represents the wall density, with a value of 1 for solid nodes and 0 for fluid nodes.

For the physicochemical problems investigated in the present work, gravity force is considered, which is a body force

$$\mathbf{F}_b = \rho \mathbf{g}. \tag{9}$$

With the cohesive force of Eq. (7) considered, the equation of state (EOS) is given by

$$p = \frac{\rho}{3} + \frac{G}{6} \psi^2. \tag{10}$$

Theoretically, different EOSs can be obtained by changing the effective mass ψ [36]. Several evaluation criteria should be considered when choosing a suitable ψ [36]. The first criterion is that the maximum density ratio between the liquid and vapor available should be as large as possible. The second criterion is that the spurious currents at the liquid-vapor interface should be as low as possible. The spurious currents are ubiquitous for most of the multiphase numerical models, which usually increase as the density ratio increases. Large spurious currents can lead to the divergence of the simulation and are also difficult to distinguish from the real flow velocities [36]. The third criterion is the stable temperature range, or the lowest reduced temperature ($T_{\min}/T_c$, with T_c the critical temperature). As the temperature is increasingly lower than T_c, the density ratio increases and the spurious currents increase. Thus the stable temperature range available is also limited by the spurious currents. The last criterion is the agreement between the mechanical stability solution and the thermodynamic theory, which is due to the thermodynamic inconsistency of the Shan-Chen pseudopotential model. This criterion is usually invoked by comparing the coexistence curves obtained from simulation results of liquid and vapor densities with the theoretical one predicted by the Maxwell equal-area construction. Yuan and Schaefer [36] thoroughly investigated several EOSs according to the above four criteria. Based on their studies, the Carnahan-Starling EOS is adopted, which generates small spurious currents, a wide stable temperature range, a high density ratio, and good agreement of the coexistence curves [36]

$$p = \rho RT \frac{1 + b\rho/4 + (b\rho/4)^2 - (b\rho/4)^3}{(1 - b\rho/4)^3} - a\rho^2, \quad (11)$$

where $a = 0.4963 (RT_c)^2 / p_c$ and $b = 0.1873 RT_c / p_c$. In the present study, we set $a = 1$, $b = 4$, $R = 1$, $T_c = 0.094$, and $\rho_c = 0.13044$ [36]. Thus ψ can be obtained by

$$\psi = \sqrt{\frac{6}{G} \left(\rho RT \frac{1 + b\rho/4 + (b\rho/4)^2 - (b\rho/4)^3}{(1 - b\rho/4)^3} - a\rho^2 - \frac{\rho}{3} \right)}. \tag{12}$$

Compared to the original $\psi = \exp(-1/\rho)$ used in the Shan-Chen model, ψ here contains a defined temperature T. Thus G becomes unimportant now and is only required to guarantee the whole term under the square root to be positive [36]. In the present study, $G = -1$.

The correct incorporation of the forcing terms into the LBM is an importance issue. The forcing scheme greatly affects the spurious currents, stable temperature range, maximum density ratio, and agreement of the coexistence curves [37–39]. Recently, Huang *et al.* [38] and Li *et al.* [39] compared different forcing schemes in the Shan-Chen pseudopotential model including that proposed by Shan and Chen [22], Guo *et al.* [40],

Ladd and Verberg's [41] and Kupershtokh *et al.* [37]. Based on the evaluation in [38,39], we adopt the exact difference method (EDM) developed by Kupershtokh *et al.* [37], which is directly derived from the Boltzmann equation. In the EDM, a source term is added on the right-hand side of the evolution equation (1),

$$\Delta f_i = f_i^{\text{eq}}(\rho, \mathbf{u}') - f_i^{\text{eq}}(\rho, \mathbf{u}), \tag{13}$$

where $\mathbf{u}$ is obtained by Eq. (5b) and $\mathbf{u}'$ equals

$$\mathbf{u}' = \mathbf{u} + \frac{\mathbf{F}\Delta t}{\rho}, \tag{14}$$

where $\mathbf{F}$ is the sum of the forces, including the force between fluid particles, the force between the fluid and solid, and the body force. By averaging the moment before and after the collision, the real fluid velocity is expressed as

$$\mathbf{u}_r = \mathbf{u} + \frac{\mathbf{F}\Delta t}{2\rho}. \tag{15}$$

There have been several studies using the single-component multiphase flow Shan-Chen model to investigate fluid flow with phase transitions. Joshi and Sun [5] adopted the model to study the multiphase flow with solid particles inside the liquid phase. In their studies, an evaporation scheme is used to obtain the isothermal evaporation process by artificially removing the vapor mass from the computational domain. Recently, Márkus and Házi [42] combined the Shan-Chen model with a heat transfer model to study the nonisothermal evaporation process. Adding a small and random density perturbation on the initial uniform density is a common numerical scheme to promote the phase transition [22,43]. Shan and Chen [22] simulated the phase transition phenomenon by adding a random perturbation of 1% on the initially uniform density field ρ_0. We investigated such a scheme in detail and found the following in the single-component multiphase Shan-Chen model. (i) The perturbation is necessary; otherwise the phase transition will not take place even when ρ_0 is extremely low. (ii) At a certain temperature, ρ_0 should be lower than a critical value. For example, we found that for $T = 0.7T_c$ [under this temperature the densities of the liquid water and vapor simulated by our code are 0.3589 and 0.00670 (in lattice units), respectively, with good agreement with the theoretical densities predicted by the Maxwell equal-area construction of 0.3572 and 0.00312], ρ_0 should be lower than 0.27, above which the phase transition cannot be activated. (iii) The higher the value of ρ_0, the lower the maximum perturbation should be; otherwise the simulation will diverge. For example, when $\rho_0 = 0.27$, the maximum perturbation should be as low as 0.1%; in contrast, when $\rho_0 = 0.1$, a stable solution is still available with a maximum perturbation as high as 5%. Since in our simulations the initial inclusion is in the liquid phase with the liquid density at the corresponding temperature, for example, 0.3572 at $T = 0.7T_c$, and the averaged density in the closed inclusion gradually decreases as the volume of the inclusion increases during the migration, the maximum perturbation should be small enough and is set as 0.1% in the present study after prior simulation tests.

B. The LB model for mass transport

There have been several studies to solve the convection-diffusion equation of solute transport using the LBM [44]. The following evolution of the LB equation is used to describe species transport [33]:

$$g_{i,k}(\mathbf{x} + c\mathbf{e}_i\Delta t, t + \Delta t) - g_{i,k}(\mathbf{x}, t)$$
$$= -\frac{1}{\tau_g}\big[g_{i,k}(\mathbf{x}, t) - g_{i,k}^{\text{eq}}(\mathbf{x}, t)\big] + J_{i,k}\Delta t S, \tag{16}$$

where $g_{i,k}$ is the concentration distribution function for k component and S the source term related to homogeneous reactions.

Note that the convection-diffusion equation is linear in velocity $\mathbf{u}$. This means that the equilibrium distributions for scalar transport need only be linear in $\mathbf{u}$ and thus lattices with fewer vectors can be used for scalar transport. Noble [45] performed a Chapman-Enskog expansion for the LB model with equilibrium distributions linear in $\mathbf{u}$ and with a reduced number of lattice velocities, recovering the advection-diffusion equations. Thus a reduced D2Q5 lattice model of the original D2Q9 model given by Eq. (3) is used by abandoning the lattice speed in the diagonal directions ($\mathbf{e}_i, i = 5 - 8$). An equilibrium distribution that is linear in $\mathbf{u}$ is adopted [33]:

$$g_{i,k}^{\text{eq}} = C_k\big[J_{i,k} + \tfrac{1}{2}\mathbf{e}_i \cdot \mathbf{u}\big], \tag{17}$$

where C is the concentration and J_i is given by [33]

$$J_i = \begin{cases} J_0, & i = 0 \\ (1 - J_0)/4, & i = 1,2,3,4, \end{cases} \tag{18}$$

where the rest fraction J_0 can be selected from 0 to 1. The equilibrium distribution function given by Eq. (17) can cover a wide range of diffusivity by adjusting J_0, which is a prominent advantage of such an equilibrium distribution [3,33]. Note that different forms of equilibrium distribution functions with the D2Q5 model are employed in the literature. For example, in the study of Huber *et al.* [46], the equilibrium distribution function is chosen as $g_i^{\text{eq}} = C[J_i + 0.5\mathbf{e}_i \cdot \mathbf{u}]$ with $J_0 = 1/3$ and $J_{1--4} = 1/6$, in the study of Chen *et al.* [47] $g_i^{\text{eq}} = C[J_i + 0.5\mathbf{e}_i \cdot \mathbf{u}]$ with $J_{0-4} = 1/5$, and in the study of Kang *et al.* [48] $g_i^{\text{eq}} = C[J_i + 0.5\mathbf{e}_i \cdot \mathbf{u}]$ with $J_0 = 0$ and $J_{1-4} = 1/4$. We point out that Eq. (16) in the present study is a general formula, which becomes that in [46] if $J_0 = 1/3$, that in [47] if $J_0 = 1/5$, and that in [48] if $J_0 = 0$. Such a general formula is also adopted in Ref. [44]. The accuracy and efficiency of the reduced D2Q5 model has been confirmed in other studies [2,3,13,33,44–49]. The concentration is obtained by

$$C = \sum g_i. \tag{19}$$

The diffusivity is related to the relaxation time by

$$D = \tfrac{1}{2}(1 - J_0)(\tau_g - 0.5). \tag{20}$$

In the present study, solid salt dissolves or precipitates only at the liquid-solid salt interface; correspondingly, the aqueous salt transports only in the liquid water and not in the vapor. Therefore, we solve the solute transport only in the liquid phase and consider the liquid-vapor interface as zero-flux boundaries. We use the following simple approach

to distinguish the liquid phase and vapor phase: If the density of a node is higher than a critical density (chosen as half of the maximum density in the system), the node is regarded as a liquid node; otherwise it is a vapor node. It is well known that as the density ratio between liquid and vapor phases becomes large, the spurious currents around the interface become large. Such large spurious currents would have unphysical effects on the mass transport and thus must be avoided or reduced. Close examination reveals that large spurious currents around the liquid-vapor phase are mainly in the vapor phase; thus such spurious currents are avoided in the present study as we solve only the mass transport in the liquid phase.

The moving liquid-vapor interface poses significant challenges to the simulation of solute transport in the liquid phase. Two issues are required to be resolved. The first issue is how to handle the concentration of the solute associated with a node that is changed from liquid phase to vapor phase, or vice versa, during the evolution of the liquid-vapor interface. This issue is discussed in Sec. III F. The second issue is that since the liquid-vapor interfaces are moving boundaries and liquid-solid boundaries are reactive boundaries for the solute transport, a unified concentration boundary condition that can handle moving and reactive boundaries is required. This issue is discussed in Sec. III G.

C. Heat transfer

In this study, the top and bottom walls of the salt are fixed as a higher temperature and a lower temperature, respectively, while the left and right wall are adiabatic walls. Based on assumption (ii) in Sec. II and assuming that the thermal properties of the salt are independent of temperature, the temperature field reduces to a linear function of distance from the top wall to the bottom wall. Under this circumstance, therefore, we simply prescribe this linear temperature distribution during the simulations. Nevertheless, if the heat transfer process is very complex and cannot be easily solved analytically, a thermal LB model also can be adopted to predict the heat transfer processes involving conjugated heat transfer between the fluid and solid phase; for more detail on simulations of this sort, the reader is referred to our recent work on coupled physicochemical processes in microreactors [49].

D. Heterogeneous reactions at the solid-liquid interface

Since the solute exists only in the liquid phase, dissolution and precipitation occur only at the liquid-solid salt interface. At the liquid-solid salt interface, the following heterogeneous chemical reaction takes place:

$$S_{aq} \rightleftharpoons S_S, \tag{21}$$

where S_{aq} and S_s represent the aqueous phase (solute) and solid phase of the salt, respectively. Obviously, local supersaturated conditions result in precipitation and local undersaturated conditions lead to dissolution. From Eq. (21) it follows that the boundary condition at the liquid-solid interface for the aqueous phase is represented by

$$D\frac{\partial C_{aq}}{\partial \mathbf{n}} = -k(1 - KC_{aq}), \tag{22}$$

where k is the reaction rate and C_{aq} is the concentration of the aqueous phase salt. The term $\mathbf{n}$ represents the surface normal that points into the fluid and K is the equilibrium constant, with higher K implying lower salt solubility. Further, K is a function of temperature, which is represented in the present study using the relatively simple relationship

$$K = (aT + b)^{-1}, \tag{23}$$

where a and b are constants. Thus, if K is high (or the solubility is low) and the right-hand side of Eq. (22) is positive, then precipitation takes place; conversely, if K is low (or the solubility is high) and the right-hand side of Eq. (22) is negative, then dissolution takes place.

E. The VOP method for dissolution and precipitation

In the VOP method, the entire domain is divided into pixels (or computational nodes). Each pixel is assigned a value representing the volume of the solid phase. At each time step, at the reactive solid-fluid interfaces, the volume of a solid node V_s with initial value of V_0 is updated by

$$\frac{\partial V_s}{\partial t} = -A V_m k (1 - KC_{aq}), \tag{24}$$

where A is the reaction area and V_m is the molar volume. Thus V_s is updated at each time step by

$$V_s(t + \Delta t) = V_s(t) - V_m k(1 - KC_{aq})\Delta t A, \tag{25}$$

where Δt is the time step and equals that in Eq. (2) in the simulation.

If V_s reaches zero, dissolution is complete and the solid node is removed and converted to a fluid node; meanwhile, the fluid flow and mass information in this new fluid node must be initialized. In contrast, when the volume of a solid node exceeds a certain threshold value, for example, if it doubles in the present study, precipitation takes place and one of the nearest-neighbor fluid nodes becomes a solid node. At the same time the volume of the original solid node is set back to V_0 and the initial volume of the new solid node is assigned as V_0. Because there may be several fluid nodes around the original solid node, several rules have been proposed by Kang *et al.* [28] to determine which one of these fluid nodes is chosen for the precipitation. In the present study, this node is simply randomly determined.

F. Treating information on nodes undergoing phase change

Figure 2 schematically shows the time evolution of the solid-liquid-vapor interfaces. During the interface evolution, the phase of a computational node may switch between liquid and solid phases (due to dissolution or precipitation) or between liquid and vapor phases (due to phase separation). Note that there is no switch between vapor and solid phases because the dissolution-precipitation process takes place only at liquid-solid interfaces. How to treat the fluid flow and mass transport information associated with computational nodes undergoing phase changes is of great importance to guarantee the mass and momentum conservation in a closed system. For example, there are multiple ways to initialize the information at a new fluid node during dissolution and to distribute the information stored at a newly added solid node into the
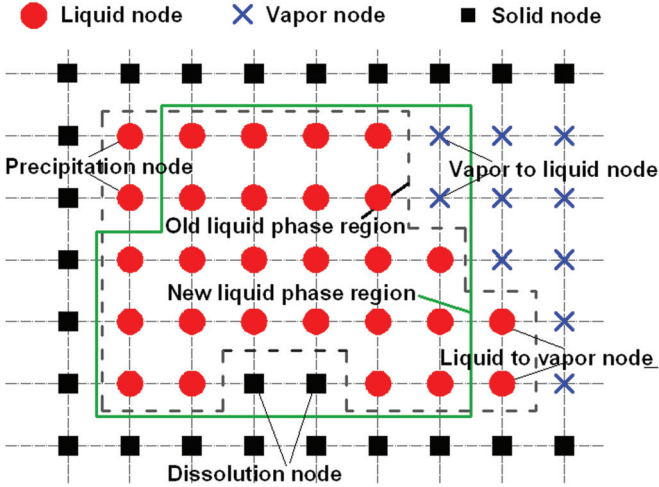
FIG. 2. (Color online) Dynamic evolution of liquid-vapor-solid interfaces during the multiphase reactive transport process. There are three types of nodes in the domain, namely, solid nodes, liquid nodes, and vapor nodes, and there are four kinds of changes of node type: namely, liquid to solid due to precipitation, solid to liquid due to dissolution, liquid to vapor, and vapor to liquid, the third and fourth of these due to evolution of the liquid-vapor interfaces. Note that there is no exchange between the vapor node and solid node as dissolution and precipitation take place only at the liquid-solid interface.

neighboring fluid nodes during precipitation. The desirable method should treat phase changes consistently and accurately while obeying basic physical laws, i.e., conservation of mass and momentum. These considerations are discussed in this section.

The switches between the solid phase and fluid phase are common in the problems of suspended particles transporting in fluid [41,50,51], dissolution and precipitation [2,9,18], and melting and solidification [46,52]. When a solid node is changed into a fluid node due to dissolution, the density as well as the velocity at this node must be initialized in a way that guarantees mass conservation of the closed system and convergence of the simulation. In this study we set the density of this new liquid node (ρ_{new}) as the averaged density of the nearest-neighbor liquid nodes and $\mathbf{u}_{new}$ as that of the corresponding solid node, namely, zero. Obviously, at each time step if m nodes are dissolved, additional fluid mass $\sum_1^m \rho_{new}$ is added into the closed system. To guarantee mass conservation of the closed system after the dissolution and precipitation step of the current time step is completed, the density of each fluid node (including the liquid nodes newly formed) is modified by

$$\rho^t(i,j) = (1+\delta)\rho^{t-\Delta t}(i,j) \frac{\sum \rho^{t-\Delta t}(i,j)}{\sum_1^m \rho_{new} + \sum \rho^{t-\Delta t}(i,j) - \sum_1^n \rho_{old}},$$

(26)

where $\sum \rho^{t-\Delta t}$ is the total density of the closed system at the former time step. Superscripts t and $t - \Delta t$ represent the current time and the former time, respectively. The term $\sum_1^n \rho_{old}$ accounts for the effects due to precipitation and will be discussed later. Note that a random perturbation δ (–0.1%, 0.1%) is also added as shown in Eq. (26) to activate the phase transition. Since the velocities of these newly created liquid

nodes are zero, (i) no additional momentum is added into the system and (ii) the distribution functions of these new fluid nodes can be initialized as the equilibrium distribution functions [13]. This scheme is reasonable because a solid node is gradually dissolved (typically requires several thousand time steps in our simulations). During this period of time, the reduction of fluid density due to the volume increase caused by dissolution has already been transferred to the entire fluid field. However, because our numerical model removes the solid node in a single time step when its volume is reduced to zero, it is reasonable to reset the entire density field at this single time step using Eq. (26) to account for the accumulated effect during the past several thousand time steps of dissolution process. This scheme not only guarantees mass and momentum conservation, but also predicts reasonable phase transition processes.

In the study of suspended particles transporting in fluid, when a fluid node is covered by a solid node, the common practice is to simply remove this fluid node from the system [50,51]. This is acceptable for open systems considered in other studies [49,50]. However, for a closed system, the mass and momentum attached to the fluid node must be transferred to the fluid region in order to guarantee mass and momentum conservation. Similar to the scheme described above for handling dissolution, the density of this fluid node is uniformly distributed over the entire flow field when it is converted to a solid node. Supposing n fluid nodes are converted at a certain time step, the total mass loss is $\sum_1^n \rho_{old}$, which is subtracted from the denominator of Eq. (26).

In the present study, we solve the solute transport equation in the liquid phase. The liquid-vapor interface is moving and computational nodes will undergo liquid-vapor phase changes. Thus it is also a requirement to handle the concentration of the solute associated with a node that is changed from the liquid phase to the vapor phase, or vice versa, during the evolution of the liquid-vapor interface (Fig. 2). The scheme similar to treating dissolution-precipitation processes is adopted here. When a vapor node is changed into a liquid node, the concentration of this node is initialized as the averaged concentrations of surrounding pre-existing liquid nodes. The newly formed liquid nodes due to two-phase interface evolution or dissolution of solid nodes cannot be included for averaging. If there is no pre-existing liquid node around the newly formed liquid node, then its concentration is set as the local saturation concentration. The solute mass associated with the newly formed liquid node is considered to be uniformly taken from all the liquid nodes and thus an equation similar to Eq. (26) is employed to reset the concentration field. When a liquid node is changed into a vapor node, its concentration is uniformly distributed over all the liquid nodes.

G. A general concentration boundary condition

For solute transport in the liquid phase, the solid-liquid interfaces are reactive boundaries and the liquid-vapor interfaces are moving boundaries. To handle these complex structured boundaries, a unified LB concentration boundary condition is required that can handle moving and reactive boundaries. Several concentration boundary conditions have
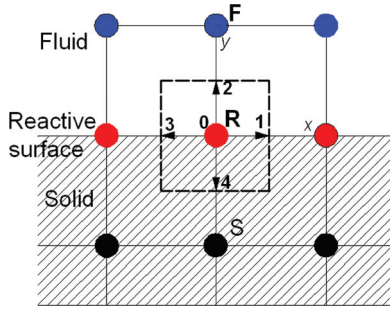
FIG. 3. (Color online) Schematic illustration of a liquid-solid (or vapor) interface node R. Here F is the fluid node and S is the solid (or vapor) node.

been developed for different boundary condition types in the literature; for a recent review, the reader is referred to [44,53]. There have also been a few studies treating reactive boundaries [9,48,53,54]. To discuss the concentration boundary conditions, a schematic illustration of the fluid-solid interface is presented in Fig. 3. Following Ref. [53], the boundary condition at this interface is

$$b_1 \frac{\partial C}{\partial \mathbf{n}} + b_2 C = b_3, \tag{27}$$

which is a general formula that can describe all three types of boundary conditions: the Dirichlet boundary condition, with $b_1 = 0$ and $b_2 \neq 0$; the Neumann boundary condition, with $b_2 = 0$ and $b_1 \neq 0$; and a mixed boundary condition, with $b_1 \neq 0$ and $b_2 \neq 0$.

Kang *et al.* [48] provided a correct expression of the concentration distribution function in terms of the corresponding concentration and its gradient

$$\sum g_i \mathbf{e}_i = C\mathbf{u} - D\nabla C. \tag{28}$$

In Fig. 3, after each streaming step, g_2 is unknown and g_4 is known; g_1 and g_3 do not affect the fluid domain and hence are not needed to calculate their values.

In the study of Kang *et al.* [48], the reactive wall is static. Kang *et al.* [48] pointed out that since g_2 enters the domain and g_4 leaves the domain, based on Eq. (28) the following equation is obtained at the reactive node R:

$$g_2 - g_4 = -\frac{D}{c}\frac{\partial C}{\partial y} = k(1 - KC). \tag{29}$$

Then they derived a relation in which the nonequilibrium portion of the distribution functions in opposite directions takes the opposite sign for a static wall, from which they obtained another equation

$$g_2 + g_4 = \left(g_2^{\text{eq}} + g_2^{\text{neq}}\right) + \left(g_4^{\text{eq}} + g_4^{\text{neq}}\right) = g_2^{\text{eq}} + g_4^{\text{eq}}. \tag{30}$$

Combining Eqs. (28) and (30), the unknown distribution g_2 can be obtained.

Zhang *et al.* [53] proposed a so-called general bounce-back scheme for concentration boundary conditions. First, they solved Eq. (27) directly to obtain the concentration at the boundary using the difference scheme

$$\frac{\partial C}{\partial n} = \frac{C_R - C_F}{|\Delta \mathbf{x}|}, \tag{31}$$

where C_R and C_F are the concentrations at interface node R and adjacent fluid node F, respectively, and $\Delta\mathbf{x}$ is the vector connecting nodes F and R. Thus

$$b_1 \frac{C_R - C_F}{|\Delta\mathbf{x}|} + b_2 C = b_3; \tag{32}$$

C_R is only unknown variable in Eq. (32) and thus can be directly solved. Zhang *et al.* then used Eq. (30) to solve the unknown g_2. It is worth mentioning that Eq. (30) holds only for static walls [44]. Therefore, the boundary condition proposed by Zhang *et al.* [53], just like the one developed by Kang *et al.* [44], can treat only static wall boundaries.

In this study, we propose to use Eq. (28) to solve the unknown distribution function after C_R is obtained from Eq. (27). For the boundary node shown in Fig. 3, the boundary condition herein can be written as

$$b_1 \frac{C_R - C_F}{c} + b_2 C = b_3, \tag{33a}$$

$$g_2 - g_4 = C_R v - \frac{D}{c}\frac{\partial C}{\partial y}. \tag{33b}$$

Equation (33a) is used to solve C_R, after which Eq. (33b) is used to solve g_2. In this way, this boundary condition treatment can handle moving boundary conditions. Note that a scheme similar to the boundary condition in the present study was adopted by Walsh and Saar [54] to construct the reactive and moving boundary condition. However, their boundary condition can treat only the Neumann boundary condition as pointed out by Zhang *et al.* [53], while our scheme can treat all three types of boundary conditions. In addition, our boundary condition based on the D2Q5 model can greatly reduce the computational burden, compared with the D2Q9 model used by Walsh and Saar [54] and Zhang *et al.* [53].

The boundary condition described by Eq. (33) can be uniformly used to treat both a reactive liquid-solid boundary and a zero-flux liquid-vapor boundary. For the static liquid-solid boundary, a precipitation or dissolution reaction described by Eq. (22) leads to the following reduced form of Eq. (33) (supposing a boundary such as that shown in Fig. 3):

$$D\frac{C_R - C_F}{c} = -k(1 - KC_R), \tag{34a}$$

$$g_2 - g_4 = -\frac{D}{c}\frac{\partial C}{\partial y}. \tag{34b}$$

In contrast, for the moving liquid-vapor boundary, there is no reaction and the concentration gradient of solute is zero. Thus Eq. (33) reduces to (supposing a boundary like that shown in Fig. 3)

$$D\frac{C_R - C_F}{c} = 0, \tag{35a}$$

$$g_2 - g_4 = C_R v. \tag{35b}$$

H. Numerical procedure

After initialization, each iteration involves the following substeps: (i) updating the fluid field using the single-component multiphase Shan-Chen LB model, (ii) solving the solute (namely, the concentration of salt in the aqueous phase) transport in the liquid water with the heterogeneous reaction at the liquid-solid interface using the LB mass

transport model, and (iii) updating the density of solid salt nodes and updating the geometry of the solid phase using the dissolution-precipitation model. For the systems considered here, the evolution of the solid geometry due to dissolution or precipitation is very slow compared to fluid flow or solute transport. Thus, at each configuration of the solid phase, the steady state of the fluid flow and mass transport can be obtained. The time step for flow and transport is kept the same by adjusting the relaxation time and J_0.

IV. VALIDATION

Our numerical model is constructed incrementally by combining different models including the multiphase flow Shan-Chen model [3,24], mass transport with homogeneous and heterogeneous reactions [13,48], and dissolution and precipitation including nucleation and crystal growth [2,18]. Since no analytical solutions or experimental results of these complex coupled nonlinear multiple physicochemical processes are available for performing quantitative comparisons with our simulation results, our validation consists of testing each of the submodels, each of which has appropriate theoretical results with which to compare to our pore-scale model.

A. Single-component two-phase flow

Several physical problems are selected for validation of the single-component multiphase Shan-Chen model. The first one is first-order phase separation. We carried out a series of simulations with different initial uniform densities added with different perturbations in a 201×201 lattice periodic system with different temperature. In this and all subsequent simulations, the relaxation time $\tau_\upsilon = 1.0$. The conclusions of simulations of the phase separation have been discussed in Sec. III A and are not repeated here.

The second comparison is the circular static liquid droplet embedded in the vapor phase in a gravity-free field. We simulate this problem using a 201×201 lattice periodic system. In the simulation, a liquid droplet with initial radius r_0 is placed at the center of the domain. The density field is initialized using the method in Ref. [38]:

$$\rho(i,j) = \frac{\rho_{\text{liquid}} + \rho_{\text{vapor}}}{2} - \frac{\rho_{\text{liquid}} - \rho_{\text{vapor}}}{2} \tanh$$
$$\times \left[\frac{2[\sqrt{(i - i_{\text{center}})^2 + (j - j_{\text{center}})^2} - r_0]}{W} \right], \quad (36)$$

where ($i_{\text{center}} = 101$, $j_{\text{center}} = 101$) is the center position of the domain, tanh is the hyperbolic tangent function, and $\tanh(x) = (e^{2x} - 1)/(e^{2x} + 1)$. Values for ρ_{liquid} and ρ_{vapor} are set as the theoretical densities predicted by Maxwell equal-area construction at the corresponding temperature. A typical steady-state density contour obtained from simulations of this problem is shown in Fig. 4(a), in which $T = 0.7T_c$ and $r_0 = 30$. To check the coexistence curves, a series of simulations is carried out by changing T while fixing r_0. The LB simulated coexistence curves are in good agreement with the theoretical one as shown in Fig. 4(b), where the discrepancy is due to the thermodynamic inconsistency of the

Shan-Chen pseudopotential model. The lowest temperature we can achieve is $0.57T_c$, which is slightly higher than that of Yuan and Schaefer [36]. Besides, to calibrate the Laplace law, a series of simulations is conducted by changing r_0 while fixing $T = 0.7T_c$. The Laplace law states that the pressure difference Δp inside and outside a liquid droplet is inversely proportional to the droplet radius

$$\Delta p = \frac{\sigma}{r}, \quad (37)$$

where σ is the surface tension coefficient. Pressure measurements are taken from the pressure profile along line AB, the horizontal centerline of the domain as shown in Fig. 4(a). A typical pressure distribution along line AB for $T = 0.7T_c$ and $r_0 = 30$ is plotted in Fig. 4(c). As shown in Fig. 4(c), Δp is calculated as the difference between the steady high pressure inside the droplet and the steady low pressure outside the droplet. Note that large fluctuations of the pressure near the liquid-vapor interface are unphysical due to a sharp change of density and are ignored when calculating Δp. Figure 4(d) plots Δp as a function of $1/r$, where the linear relationship can be clearly observed. The value of σ obtained by linear fitting of our simulation results is 0.0152, which is in acceptable agreement with the theoretical value of 0.009386, compared to the available numerical study in the literature [38]. The discrepancy is also due to the thermodynamic inconsistency [38].

The last problem for validation of two-phase flow is the equilibrium contact angle for a liquid droplet on a flat and uniform solid wall. The contact angle is usually considered as a measure of the solid surface wettability. A surface is wetting or hydrophilic if the contact angle $\theta < 90°$ and liquid tends to spread as a film on the solid surface. In contrast, the surface is nonwetting or hydrophobic if $\theta < 90°$ and liquid tends to form a droplet on the solid surface. We carried out a series of simulations in which an initially semicircular static droplet is placed on a horizontal solid surface and w is changed in the range from -0.1 to ~ 0.1 to obtain different contact angles. The simulations are performed in a 201×201 lattice system with the top and bottom boundaries as solid walls and the left and right boundaries as periodic boundaries. Figure 5 shows the relationship between w and the predicted contact angles for the case of $T = 0.7T_c$ and $r_0 = 30$. The insets in Fig. 5 show typical droplets with different contact angles. The relationship between the contact angle and w is almost linear, agreeing with the simulation results in Ref. [55].

B. Mass transport

Two reactive transport problems with analytical solutions are adopted to validate our mass transport LB model and the concentration boundary condition. The first reactive transport problem for validation is species diffusion in a channel with surface reaction [48]. Species A with constant concentration C_0 diffuses into a channel of size $a \times b$ and reacts at the top surface with first-order linear kinetics. On the bottom surface of the channel there is no reaction. Both the top and bottom walls are static walls. The boundary condition at the right wall is nonflux. For the details of the governing equations and analytical solution for such a reactive transport problem, the
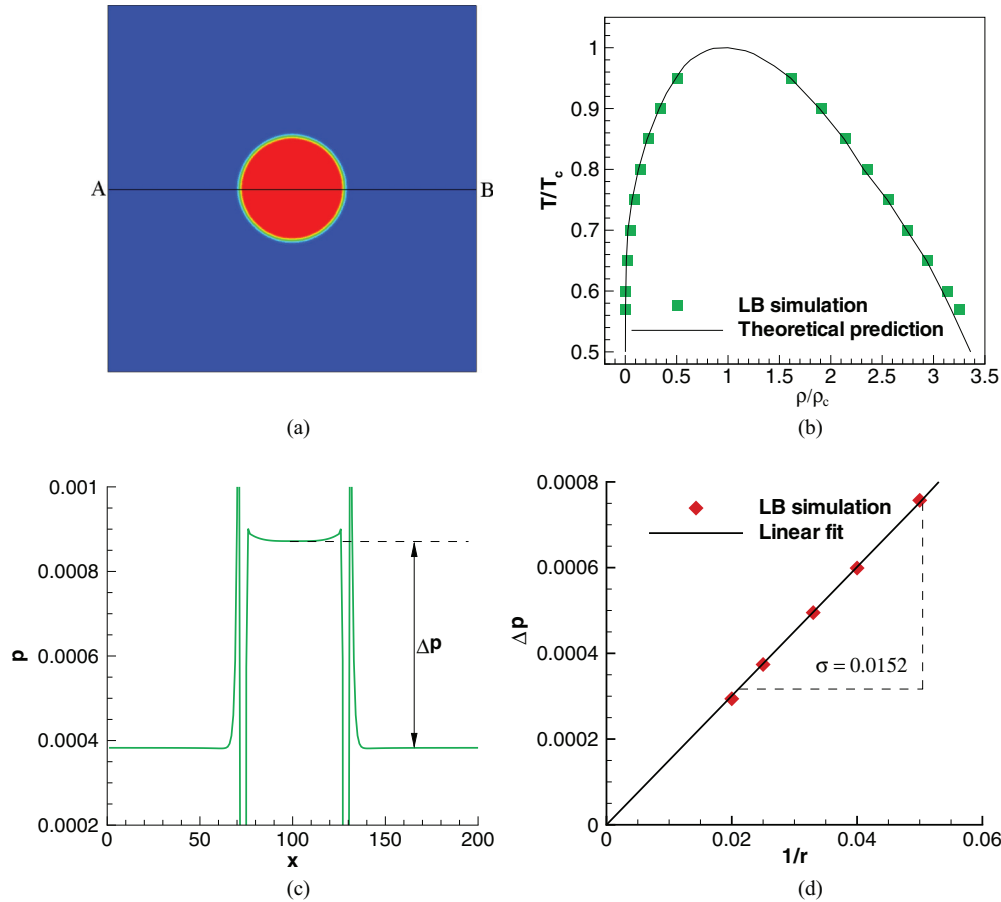
FIG. 4. (Color online) Simulation results of a circular static liquid droplet embedded in the vapor phase in a gravity-free field using a 201×201 lattices periodic system. (a) Steady-state density contours for the case at $T = 0.7T_c$ and with the initial droplet radius of 30 lattices. (b) Comparison of coexistence curves obtained from LB simulations with the theoretical one predicted by Maxwell equal-area construction. The initial droplet radius is 30 lattices. (c) Pressure distribution along the horizontal center of the computational domain. The initial droplet radius is 30 lattices and $T = 0.7T_c$. (d) Summary of LB results for the droplet with different radius and calibration of the Laplace law at $T = 0.7T_c$.
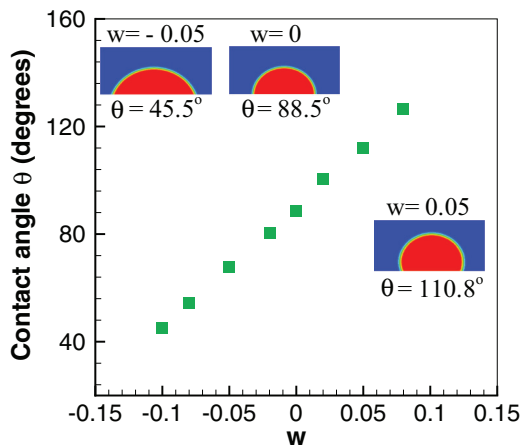
FIG. 5. (Color online) Simulation results of different equilibrium contact angles for a liquid droplet on a flat and uniform solid wall with different liquid-solid strength w. The insets show droplets with different contact angles. The system is a gravity-free field with top and bottom solid walls and periodic left and right boundaries. The system is discretized by 201×201 lattices. Here $T = 0.7T_c$ and $r_0 = 30$.

reader is referred to our previous studies [48]. The top wall is a static reactive boundary and is handled using the present concentration boundary condition. Figure 6 compares the contours of the normalized concentration C/C_0 obtained from simulations with those obtained from the analytical solution. In Fig. 6, two cases are presented with Damköhler number ($\text{Da} = kb/D$, representing the relative strength of reaction to diffusion, where k is the reaction rate of the first-order linear kinetics) values 50 and 5. Other parameters are $a = 100 \, \mu\text{m}$, $b = 100 \, \mu\text{m}$, $C_0 = 0$, $D = 3 \times 10^{-5} \, \text{m}^2\text{s}^{-1}$, and $J_0 = 0.2$. The computational domain is discretized by 101×101 lattices. As shown in Fig. 6, excellent agreement is obtained between simulation results and the analytical solutions.

The second reactive transport problem for validation is diffusion in a channel with bulk reaction [3]. Species A enters a channel with size $a \times b$ from the left inlet with concentration $C_{\text{in}} = 1$ and leaves the channel at the right outlet with concentration $C_{\text{out}} = 0$. The solvent flows with a uniform constant horizontal velocity u and the transport of species A does not affect the flow field. The bulk reaction of A takes place in the entire domain with bulk reaction rate $k \, (\text{s}^{-1})$. Thus the left and right walls are moving boundaries with known
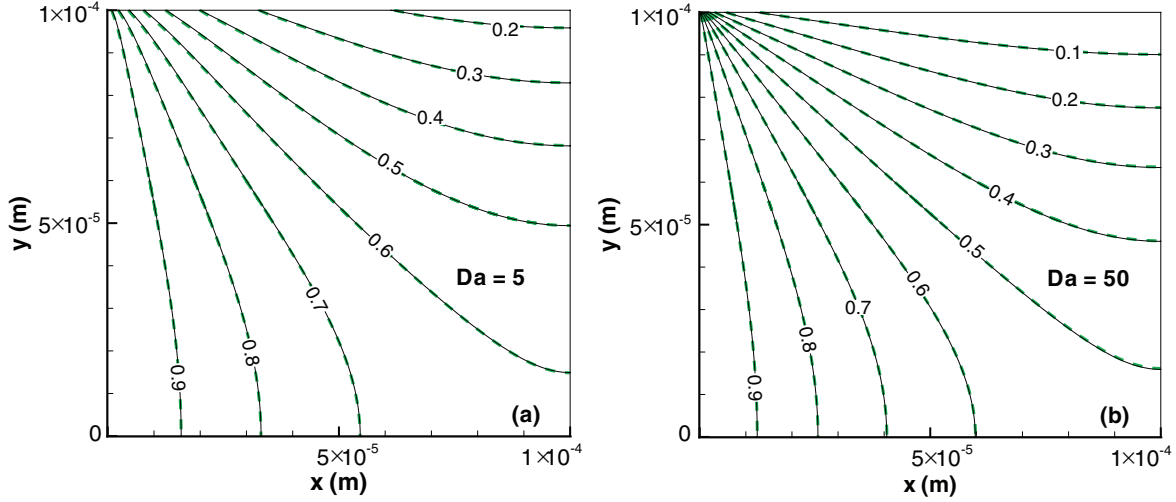
FIG. 6. (Color online) Contours of concentration at steady state for (a) Da = 5 and (b) Da = 50. The solid line and the dashed line are the analytical solution and simulation results, respectively. The size of the channel is 100×100 μm. The first-order linear kinetic reaction occurs on the top surface at $y = 100$ μm. Other parameters are $C_0 = 0$, $D = 3 \times 10^{-5}$ m^2 s^{-1}, and $J_0 = 0.2$.

concentration. The problem is essentially a one-dimensional problem. For details of the governing equations and analytical solution for this reactive transport problem, the reader is referred to our previous studies [3,13]. Figure 7 shows the simulation results for different values of Pe (Pe = ub/D, representing the relative strength of convection to diffusion) and different k. In Fig. 7, $a = 200$ μm, $b = 120$ μm, $D = 1 \times 10^{-8}$ m^2 s^{-1}, and $J_0 = 0.2$. The computational domain is discretized by 101×61 lattices. Figure 7(a) compares the simulation results of the steady-state profile of C along the x axis with the analytical solutions for different Pe, with $k = 0$. It can be seen in Fig. 7(a) that for all the cases the simulation results agree well with the analytical solutions. Figure 7(b) compares the simulation results with the analytical solutions for different reaction rate constants k for the Pe = 3 case. Again the simulation results show excellent agreement with

the analytical solutions, further validating our mass transport LB model and the present concentration boundary condition.

V. RESULTS AND DISCUSSION

A. Thermal migration of the inclusion

In this section we apply our numerical model to the study of thermal migration of a brine inclusion in a single salt crystal. The computational domain is shown in Fig. 1, which is a salt crystal containing a brine inclusion at the center. The sizes of the salt crystal and the inclusion are $L \times H = 1 \times 1$ cm^2 and $A \times B = 0.2 \times 0.2$ cm^2, respectively. The system is discretized by 202×202 lattices. Initially, the system is set at a uniform temperature $T_0 = 0.7T_c$ and the inclusion is filled with liquid brine with density $\rho_1 = 0.3572$ (the liquid
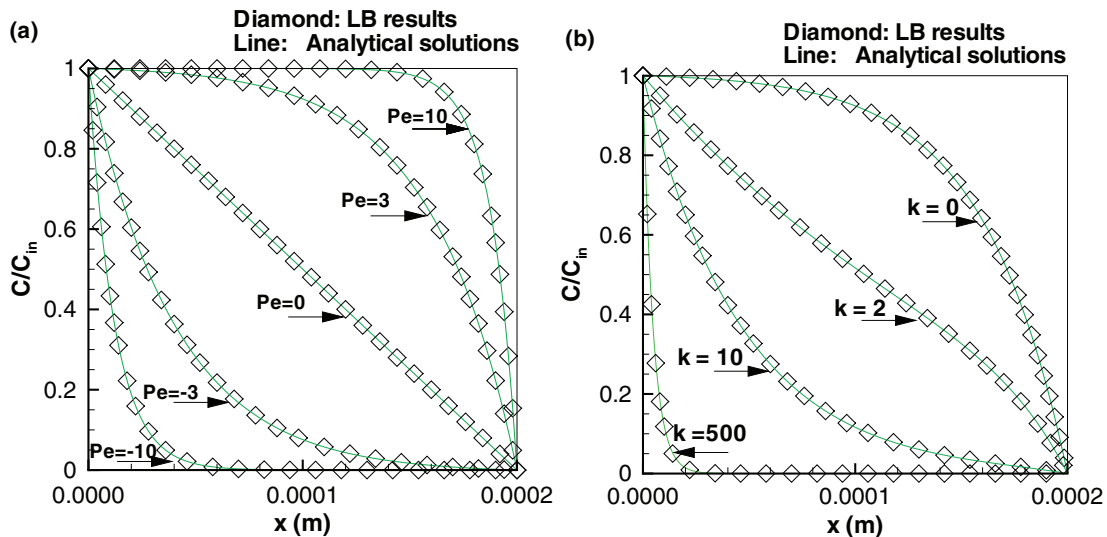
FIG. 7. (Color online) Concentration in the x direction at steady state for (a) different Pe with $k = 0$ and (b) different k for the Pe = 3 case. Solid lines and diamonds are the analytical solution and simulation results, respectively. The size of the channel is 200×100 μm. Other parameters are $D = 1 \times 10^{-8}$ m^2 s^{-1} and $J_0 = 0.2$. The computational domain is discretized by 101×61 lattices.
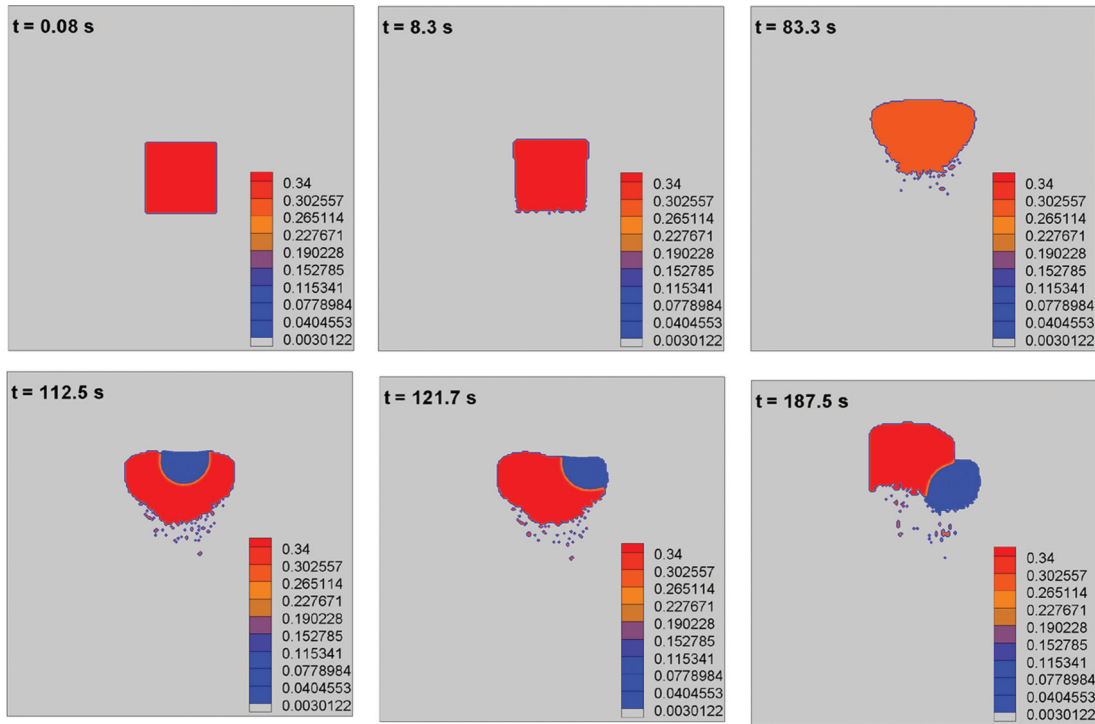
(a)
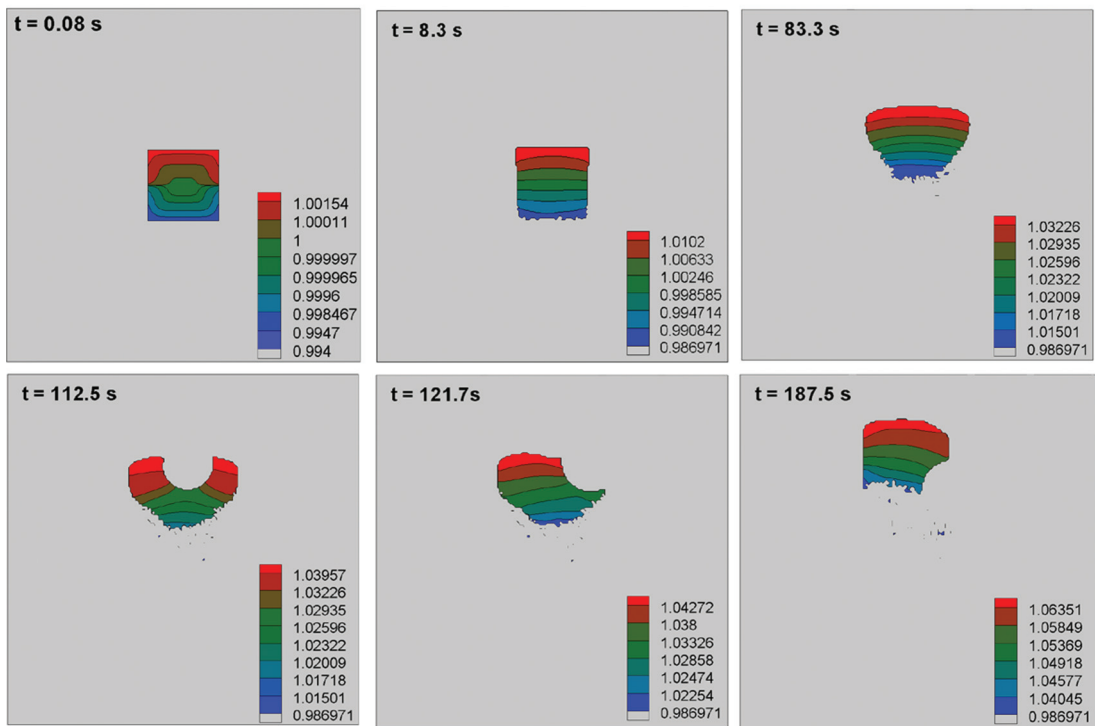
(b)

FIG. 8. (Color online) Simulation results of the thermal migration of the inclusion in the salt crystal: (a) time evolution of the density field in the inclusion and (b) time evolution of the aqueous salt concentration.

density at $T_0 = 0.7 T_c$). Then the salt crystal is subjected to a temperature gradient with $T_H = 10 + T_0$ at $y = 1$ cm and $T_L = -10 + T_0$ at $y = 0$ cm. Based on the discussion in Sec. III C, the analytical temperature distribution is linear, with $T = T_L + (T_H - T_L) \, y / H$, which is symmetrical about

$y = H/2$, where $T = T_0$. The terms a and b in Eq. (22) are taken to be 1×10^{-4} and 0.952, respectively. The kinetic viscosity is $\upsilon = 1 \times 10^{-6}$ m^2 s^{-1}, with corresponding relaxation time $\tau = 1.0$, and the diffusion coefficient of salt in water is $D = 9 \times 10^{-8}$ m^2 s^{-1} with corresponding J_0 and τ in Eq. (19)

as 0.9 and 0.8, respectively. Setting the relaxation times and J_0 in this way leads to equal time in each time step for fluid flow and mass diffusion. Other parameters for simulations are $V_m = 0.625 \times 10^{-12}$ m^3 mol^{-1} and $k = 9 \times 10^{-5}$ m^3 s^{-1}. The contact angle between liquid water and the solid salt is about 78°, which is relatively hydrophilic. For fluid flow, the nonslip boundary conditions are applied on all the solid-fluid interfaces that are obtained using the bounce-back scheme in LBM. Dissolved salt transports only in the liquid phase and reacts at the liquid-solid interface, where the dissolution-precipitation process takes place. The present concentration LB boundary condition for mass transport developed in Sec. IV B is employed on the reactive liquid-solid boundaries and the moving liquid-vapor boundaries.

The thermal migration of the inclusion is shown in Fig. 8, which displays the time evolution of the shape of the inclusion as well as the density field inside the inclusion in Fig. 8(a) and corresponding concentration of the solute in Fig. 8(b). The time required for this simulation is about three days on a Dell T7400 Workstation with eight processor cores (Intel Xeon E5420) and 3 GB of memory (the current two-dimensional computer code is not parallel and runs only on a single processor core). Subjected to the temperature gradient, the solute concentration at the bottom of the inclusion is supersaturated, while that at the top of the inclusion it is undersaturated. Therefore, the salt precipitates at the bottom of the inclusion (cold sites) and dissolves at the top of the inclusion (hot sites) ($t = 0.08$ and 8.3 s). Such microevolution of the geometry of the inclusion leads to the macro-observable migration of the inclusion ($t = 0.08$–83.3 s). Since the migration is towards the hot site and the solubility gradually increases, the amount of dissolution is larger than the amount of precipitation, leading to a volume increase of the inclusion during migration. This is shown in Fig. 9, which plots the volume of the inclusion with time, where the volume is normalized by the initial volume of the inclusion. Because the inclusion is a closed system, a volume increase
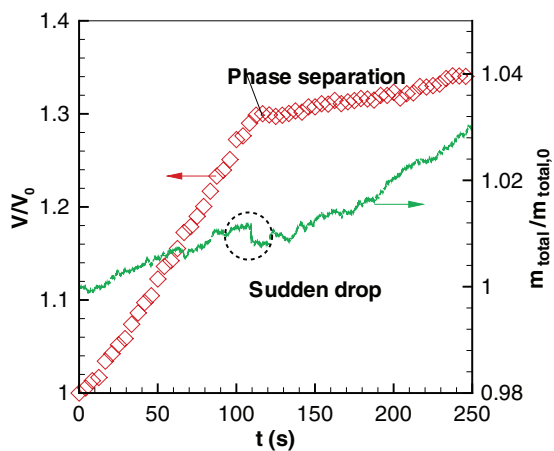
FIG. 9. (Color online) Variation of inclusion volume and total density of fluid with time. The volume is normalized by the initial volume of the inclusion. The inclusion volume increases due to a greater amount of dissolution relative to precipitation. The rate of the volume increase slows down after phase separation takes place. The mass conservation in the closed inclusion is acceptable, with a maximum relative change of 3.02% in 250 s.

leads to decreased fluid density. For example, at $t = 83.3$ s, the density of the fluid is reduced to about 0.29, compared to the initial density 0.35. When the density of the fluid is dropped to a critical value (0.27 for $T = 0.7T_c$, as mentioned in Sec. III A), the phase separation takes place ($t = 112.5$ s), with the fluid partitioning into liquid and vapor phases with densities of 0.3572 and 0.00312, respectively. As shown in Fig. 9, the rate of the increase of the inclusion volume slows after the phase separation occurs. This occurs because the solute once in the entire inclusion now is concentrated in the liquid phase during the short time of phase separation, leading to a higher concentration of solute in the liquid phase. The higher solute concentration facilitates the precipitation while slowing down the dissolution, leading to a reduced rate of the inclusion volume growth. In addition, the reactive surface area for dissolution-precipitation reactions, which take place only at liquid-solid interfaces, decreases [$t = 112.5$–187.5 s in Figs. 8(a) and 8(b)]. In addition, from the set of images in Fig. 8 it can be seen that there are many extremely small inclusions left behind in the wake of the inclusion. This is due to the randomness of the precipitation process. Finally, it is worth mentioning that during the entire process the fluid flow in the closed system is extremely slow, which leads to the dominance of diffusion over advection for mass transport in the inclusion. The concentration profiles in Fig. 8 are consistent with this interpretation.

Figure 9 also presents the variation of total fluid density in the inclusion with time. The mass conservation constraint is reasonably satisfied, with a maximum relative variation of the density of 3.02% in 250 s, indicating that our scheme of handling information associated with nodes undergoing phase change is reliable. Note that there is sudden drop of the total density when phase separation of liquid-vapor phases occurs, as shown in Fig. 9. This is because the current Shan-Chen model and the force scheme employed in the present study introduce an unphysical source term into the mass conservation equation, as reported in Ref. [39]. Since the source term is the time derivative of the forces, it is relatively large when phase separation takes place, which generates forces between liquid and vapor phases in a very short time, thus resulting in the sudden drop of total density.

Overall, the macrothermal migration of the inclusion and the microscopic complex coupled multiple physicochemical processes including multiphase flow with phase separation, mass transport, surface reactions, and dissolution and precipitation are well captured by our pore-scale model.

B. Effects of initial inclusion size and temperature gradient

We now present parameter sensitivity studies examining the effects of initial inclusion size and the temperature gradient on the thermal migration processes. To simplify the discussion, we ignore the phase separation and assume a liquid phase during the entire migration process. Since the migration of the brine inclusion is very slow and the fluid flow inside the inclusion is inconsequential, this analysis considers only the mass transport and dissolution-precipitation subprocesses. Figure 10(a) shows the relationship between inclusion volume and time for different initial inclusion size for simulations in which the inclusion travels from the starting point to the top

(a)

(b)
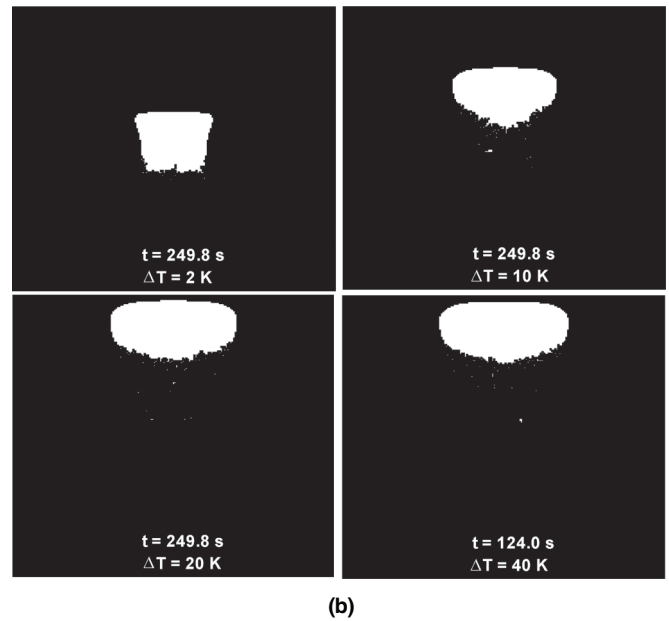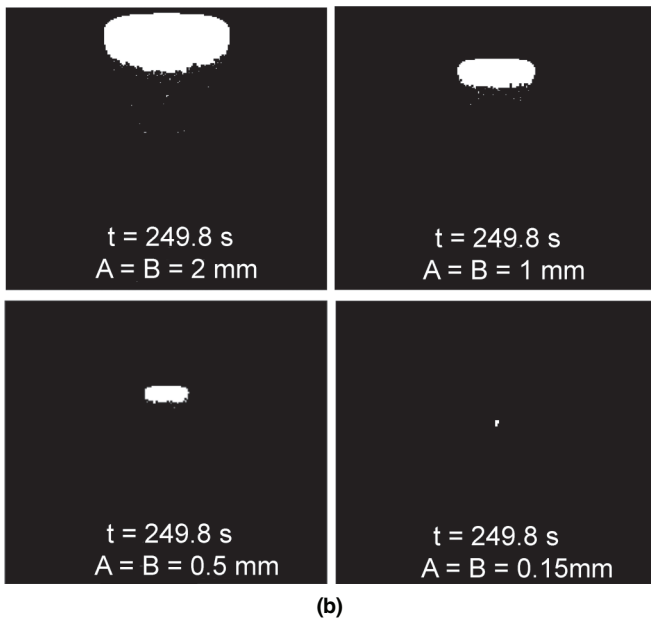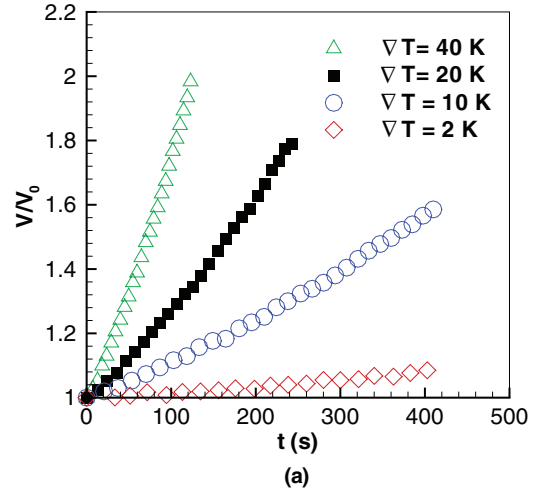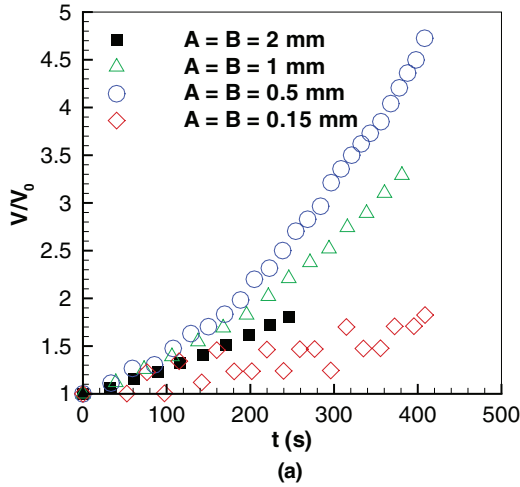
FIG. 10. (Color online) Effects of inclusion size on the migration process: (a) relationship between inclusion volume and time and (b) inclusion shape and location at a given time (249.8 s).

(a)

(b)

FIG. 11. (Color online) Effects of temperature gradient on the migration process: (a) relationship between inclusion volume and time and (b) inclusion shape and location at a given time (249.8 s, except for the leftmost figure, for which the inclusion reaches the boundary at 124 s).

boundary of the salt crystal. Figure 10(b) shows the inclusion geometries and positions for different initial inclusion size at $t = 249.8$ s. In the simulations, all the parameters are the same as in the preceding section, except the initial inclusion size. Figure 10(a) shows that the volume increase depends strongly on the inclusion size such that the larger inclusions exhibit a smaller relative volume increase. For example, for the inclusion with an initial size of 0.5 mm, the ratio between the final volume and initial volume is nearly 5, while for the inclusion with an initial size of 2 mm, the corresponding ratio is only about 1.7. This is due to more efficient and quicker mass transport from hot sites to cold sites for smaller inclusions. In addition, the macromigration velocity is larger for larger inclusions, as shown in Fig. 10(b). For example, the time required for the inclusion to reach the top boundary of the salt crystal is about 250 s for the 2-mm inclusion, while for the 0.5-mm inclusion the travel time is almost 400 s. However, in the limit of very small inclusions, such as those with a size

of 0.15 mm, the volume variation is small [the oscillation in Fig. 10(a) is due to the small initial inclusion size and model discretization issues in which one lattice of dissolution or precipitation leads to large V/V_0] and migration is extremely slow. This is because the concentration difference required for dissolution and precipitation cannot be established in such a narrow space due to the tiny temperature difference across that space. Therefore, there is rare dissolution and precipitation and thus the inclusion is almost static. Such phenomena are consistent with the conclusion in Ref. [31] that at a given thermal gradient there is a critical inclusion size under which the inclusion velocity becomes very small.

Figure 11(a) shows the relationship between the inclusion volume and time and Fig. 10(b) shows the inclusion geometries and position at a certain time for different temperature gradients. The volume variation and the macromigration

velocity are larger for larger temperature gradients. This is expected, as the larger temperature gradient leads to larger solubility differences and thus a greater driving force for dissolution-precipitation driven inclusion migration. Similar to the phenomenon of a critical inclusion size described above, there is a critical temperature gradient at which the inclusion velocity becomes very small. As shown in Fig. 11, for ΔT of 2 K, the inclusion is almost static after some dissolution and precipitation at the initial stage.

VI. CONCLUSION

Multiphase flow and reactive transport with moving solid-fluid interfaces are widespread in nature and industrial systems. In this paper, a pore-scale model based on the LBM was developed to investigate the coupled multiple physicochemical processes including multiphase flow with phase transitions, heat transfer, mass transport, surface chemical reactions, dissolution and precipitation, and dynamic evolutions of the pore-scale geometries of the solid phase. The single-component multiphase Shan-Chen LB model [22,23] was used to simulate the liquid-vapor two-phase flow, the mass transport LB model with a general form of equilibrium function [33] was used to account for mass transport, and the VOP method was adopted to describe dissolution and precipitation [28].

The scheme of adding a small and random density perturbation to obtain phase separation of a fluid system with initial uniform density ρ_0 was investigated in detail and it was found that (i) at certain temperature, ρ_0 should be lower than a critical value, above which the phase transition cannot be activated, and (ii) the higher the value of ρ_0, the lower the maximum perturbation should be, otherwise the simulation will be divergent. In addition, a scheme was developed for handling the density, velocity, and concentration associated with a node undergoing phase change between liquid-solid phases or liquid-vapor phases, which was designed to ensure mass and momentum conservation in a closed system. In addition, a general LB concentration boundary condition was also developed. The present LB concentration boundary condition can handle concentration boundaries with the general form

$b_1 \partial C / \partial \mathbf{n} + b_2 C = b_3$ and the boundaries can be moving and can have complex structures. Two reactive transport problems were employed to validate the present general LB concentration boundary condition and the simulation results are in good agreement with the corresponding analytical solutions.

The pore-scale model was used to simulate the thermally driven migration of a brined inclusion in a salt crystal. The macrothermal migration of the inclusion and the microscopic coupled multiple physicochemical processes (multiphase flow with phase separations, mass transport, surface reactions, and dissolution-precipitation processes) are well captured by our pore-scale model. The effects of the initial inclusion size and temperature gradient on the migration process were investigated. It was found that variation of the volume of the inclusion is larger for smaller inclusions due to more efficient mass transport from hot sites to cold sites in the smaller closed spaces of a smaller inclusion. In addition, the macromigration velocity is larger for larger inclusions. However, when the inclusion is extremely small, the concentration difference required for dissolution and precipitation cannot be established in the extremely narrow space of the small inclusion and thus the inclusion is almost static. With respect to the temperature gradient, the volume variation and the macromigration velocity are larger for larger temperature gradients, due to the larger solubility difference, which leads to greater amounts of dissolution and precipitation. However, for a given inclusion size, there is a critical temperature gradient below which the inclusion does not migrate.

Further work would include instigating the behavior of multiple brine inclusions in salt crystals with more complex pore structures and temperature fields, extending the present model to three dimensions, and incorporating the pore-scale model results into continuum models.

[1] Q. Kang, P. Lichtner, H. Viswanathan, and A. Abdel-Fattah, Transp. Porous Media **82**, 197 (2010).

[2] L. Chen, Q. Kang, Y.-L. He, and W.-Q. Tao, Langmuir **28**, 11745 (2012).

[3] L. Chen, H.-B. Luan, Y.-L. He, and W.-Q. Tao, Int. J. Therm. Sci. **51**, 132 (2012).

[4] L. Chen, T.-F. Cao, Z.-H. Li, Y.-L. He, and W.-Q. Tao, Int. J. Hydrogen Energ. **37**, 9155 (2012).

[5] A. S. Joshi and Y. Sun, Phys. Rev. E **82**, 041401 (2010).

[6] M. R. Kamali, S. Sundaresan, H. E. A. Van den Akker, and J. J. J. Gillissen, Chem. Eng. J. **207-208**, 587 (2012).

[7] P. Zhou and C. W. Wu, J. Power Sources **195**, 1408 (2010).

[8] Q. Kang, D. Zhang, and S. Chen, J. Geophys. Res. **108**, B10 (2003).

[9] Q. Kang, D. Zhang, S. Chen, and X. He, Phys. Rev. E **65**, 036318 (2002).

[10] L. Luquot and P. Gouze, Chem. Geol. **265**, 148 (2009).

[11] X. Li, H. Huang, and P. Meakin, Water Resour. Res. **44**, W12407 (2008).

[12] Y. Nagatsu, Y. Kondo, Y. Kato, and Y. Tad, J. Fluid Mech. **625**, 97 (2009).

[13] L. Chen, H. Luan, Y. Feng, C. Song, Y.-L. He, and W.-Q. Tao, Int. J. Heat Mass Transfer **55**, 3834 (2012).

[14] R. Middleton, G. Keating, P. Stauffer, A. Jordan, H. Viswanathan, Q. Kang, W. Carey, M. Mulkey, E. Sullivan, S. Chu, R. Esposito, and T. Meckel, Energy Environ. Sci. **5**, 7328 (2012).

[15] S. Molins, D. Trebotich, C. I. Steefel, and C. Shen, Water Resour. Res. **48**, W03527 (2012).

[16] L. Li, C. A. Peters, and M. A. Celia, Adv. Water Resour. **29**, 1351 (2006).

[17] D. Kim, C. A. Peters, and W. B. Lindquist, Water Resour. Res. **47**, W01505 (2011).

[18] Q. Kang, D. Zhang, P. C. Lichtner, and I. N. Tsimpanogiannis, Geophys. Res. Lett. **31**, L21604 (2004).

[19] A. M. Tartakovsky, P. Meakin, T. D. Scheibe, and R. M. Eichler West, J. Comput. Phys. **222**, 654 (2007).

[20] A. M. Tartakovsky, G. Redden, P. C. Lichtner, T. D. Scheibe, and P. Meakin, Water Resour. Res. **44**, W06S04 (2008).

[21] N. S. Martys and H. Chen, Phys. Rev. E **53**, 743 (1996).

[22] X. Shan and H. Chen, Phys. Rev. E **47**, 1815 (1993).

[23] X. Shan and H. Chen, Phys. Rev. E **49**, 2941 (1994).

[24] Q. Kang, D. Zhang, and S. Chen, J. Fluid Mech. **545**, 41 (2005).

[25] H. Luo, M. Quintard, G. Debenest, and F. Laouafa, Comput. Geosci. **16**, 913 (2012).

[26] H. Huang, P. Meakin, and M. Liu, Water Resour. Res. **41**, W12413 (2005).

[27] D. Yu and A. J. C. Ladd, J. Comput. Phys. **229**, 6450 (2010).

[28] Q. Kang, P. C. Lichtner, and D. Zhang, J. Geophys. Res. **111**, B05203 (2006).

[29] H. Yoon, A. J. Valocchi, C. J. Werth, and T. Dewers, Water Resour. Res. **48**, W02524 (2012).

[30] A. Parmigiani, C. Huber, O. Bachmann, and B. Chopard, J. Fluid Mech. **686**, 40 (2011).

[31] D. R. Olander, A. J. Machiels, M. Balooch, and S. K. Yagnik, J. Appl. Phys. **53**, 669 (1982).

[32] B. A. Robinson, N. Z. Elkins, and J. T. Carter, Nucl. Technol. **180**, 122 (2012).

[33] S. P. Sullivan, F. M. Sani, M. L. Johns, and L. F. Gladden, Chem. Eng. Sci. **60**, 3405 (2005).

[34] P. L. Bhatnagar, E. P. Gross, and M. Krook, Phys. Rev. **94**, 511 (1954).

[35] Y. H. Qian, D. d'Humiéres, and P. Lallemand, Europhys. Lett. **15**, 603 (1991).

[36] P. Yuan and L. Schaefer, Phys. Fluids **18**, 042101 (2006).

[37] A. L. Kupershtokh, D. A. Medvedev, and D. I. Karpov, Comput. Math. Appl. **58**, 965 (2009).

[38] H. Huang, M. Krafczyk, and X. Lu, Phys. Rev. E **84**, 046710 (2011).

[39] Q. Li, K. H. Luo, and X. J. Li, Phys. Rev. E **86**, 016709 (2012).

[40] Z. Guo, C. Zheng, and B. Shi, Phys. Rev. E **65**, 046308 (2002).

[41] A. J. C. Ladd and R. Verberg, J. Stat. Phys. **104**, 1191 (2001).

[42] A. Márkus and G. Házi, Phys. Rev. E **83**, 046705 (2011).

[43] Y. Gan, A. Xu, G. Zhang, P. Zhang, and Y. Li, Europhys. Lett. **97**, 44002 (2012).

[44] H.-B. Huang, X.-Y. Lu, and M. C. Sukop, J. Phys. A: Math. Theor. **44**, 055001 (2011).

[45] D. R. Noble, Ph.D thesis, University of Illinois at Urbana-Champaign, 1997.

[46] C. Huber, A. Parmigiani, B. Chopard, M. Manga, and O. Bachmann, Int. J. Heat Fluid Flow **29**, 1469 (2008).

[47] S. Chen, J. Tölke, S. Geller, and M. Krafczyk, Phys. Rev. E **78**, 046703 (2008).

[48] Q. Kang, P. C. Lichtner, and D. Zhang, Water Resour. Res. **43**, W12S14 (2007).

[49] L. Chen, Q. Kang, Y.-L. He, and W.-Q. Tao, Int. J. Hydrogen Energ. **37**, 13943 (2012).

[50] K. Connington, Q. Kang, H. Viswanathan, A. Abdel-Fattah, and S. Chen, Phys. Fluids **21**, 053301 (2009).

[51] C. Aidun, Y. Lu, and E.-J. Ding, J. Fluid Mech. **373**, 287 (1998).

[52] S. Chakraborty and D. Chatterjee, J. Fluid Mech. **592**, 155 (2007).

[53] T. Zhang, B. Shi, Z. Guo, Z. Chai, and J. Lu, Phys. Rev. E **85**, 016701 (2012).

[54] S. D. C. Walsh and M. O. Saar, Phys. Rev. E **82**, 066703 (2010).

[55] P. Yuan, Ph.D. thesis, School of Engineering, University of Pittsburgh, 2005.